



Exploring the spectroscopic and I-V-T characteristics advancements of cadmium zinc tungsten phosphate diode

A. M. Mansour¹ · Amany M. El Nahrawy¹ · Ali B. Abou Hammad¹

Received: 14 January 2024 / Accepted: 16 April 2024
© The Author(s) 2024

Abstract

This research accomplished the growth of cadmium zinc tungsten phosphate (CZWP) thin films on both glass and p-Si substrates, employing the sol–gel spin coating method. The sol–gel technique offers a versatile and controlled approach for fabricating nanomaterials with tailored properties. The structural and morphological analyses, conducted through XRD and FE-SEM, provided comprehensive insights into the nature of the films. The optical properties, absorbance behavior, energy gap, refractive indices, dielectric, conductivity, and electronegativity, underwent meticulous examination through UV–Vis spectroscopy. The X-ray diffraction analysis of the zinc cadmium tungsten phosphate diode reveals diffraction lines indicative of a nanostructure featuring a monoclinic-phase $\text{Zn}_2\text{P}_2\text{O}_7$ and $\text{Cd}_3\text{P}_6\text{O}_{28}$. Furthermore, SEM analysis confirms a nanoporous morphology with a nanograpes-like structure in the successful crystalline structure of the cadmium zinc tungsten phosphate nanostructure. The optical absorption studies, covering a wavelength range from 190 to 1500 nm, unveiled both direct and indirect energy band gaps, measuring 4.14 and 3.77 eV, respectively. A rigorous analysis of the I-V-T characteristics for the CZNP/p-Si junction in dark mode led to the identification of key parameters, including the transport ideality factor, barrier height, and series resistance.

Keywords Cadmium zinc tungsten phosphate · Sol–gel · XRD · SEM · Optical · Junction

1 Introduction

Recent attention on semiconductor-based energy systems centers on their high energy density and zero carbon emissions [1, 2]. Efficient charge transfer in a single semiconductor enhances optoelectronic and catalytic efficiency, but challenges arise due to recombination rate and photo-corrosion [3]. Advancements focus on constructing heterostructure semiconductor materials to minimize recombination and boost storage activity. Wide-bandgap semiconductors play a key role in satisfying the increasing demand for shorter-wavelength photonic devices and high-power electronic devices [4]. Phosphate compounds, especially, exhibit non-linear optical features, luminescence, and anti-corrosion properties [5]. With the right dopant and growth conditions, the host crystal's characteristics can be altered.

Recent interest in semiconducting oxide substances, specifically ZnO-based thin films, is fueled by their remarkable structural, optical, and electrical characteristics. These films, with a broadband gap of 3.30 eV, shine in applications spanning electronics, optics, photovoltaics, and various optoelectronic devices [6–8].

Zinc oxide (ZnO) and cadmium sulfide (CdS) films are capturing attention across scientific, industrial, and technological domains, finding applications in sensors, solar cells, and thin films [9]. The increasing interest underscores the need for economical and simple techniques to prepare extensive films, especially crucial in advancing solar cell applications [9]. Breakthroughs in high-quality growth enhance the significance of these materials. Despite ZnO's wide bandgap (3.4 eV), it hasn't received equal attention, possibly due to its perceived value only in a polycrystalline state [10, 11]. Polycrystalline ZnO finds diverse applications in cosmetic powders, piezoelectric transducers, varistors, phosphors, and transparent conducting films [11]. Recent advancements include large-scale bulk growth [12] and epitaxial methods yielding exceptional materials. Successful quantum well growth has been achieved through alloying with Mg or Cd

✉ A. M. Mansour
amamansour@gmail.com; ae.mansour@nrc.sci.eg

¹ Physics Research Institute, National Research Centre, 33 El-Bohouth St., Dokki, Giza 12622, Egypt

[13]. Through alloying ZnO with CdO, Cd²⁺ ions play a dual role by evenly replacing Zn²⁺ ions or occupying interstitial positions within the ZnO lattice [14]. Notably, the ionic radii for zinc and cadmium ions stand at 0.074 and 0.097 nm, respectively [15]. The introduction of Cd ions, with their larger radius, induces lattice distortion within the ZnO lattice system. This distortion may limit the electrical structure of the ZnO binary system, potentially leading to a reduction in the band gap of the ZnO thin film [15]. Despite this, the optical characteristics of ZnO are enhanced with Cd addition, making it an even more appealing material for optoelectronic devices [15]. Phosphate composites are great at hosting lots of active ions without losing their special properties [16]. Lately, people are really into composites with extra transition metals because they can do cool things like conduct electricity and make glass look colorful [16]. Cadmium, one of these metals, is like a coloring tool, helps things separate, and works well in solar cells that use tiny particles. Also, cadmium helps in making glass with quantum dots, but it wasn't known much about the glass structure yet [16]. The architecture of phosphate composites is commonly articulated as a network of phosphate tetrahedra, intricately linked through covalent bonding of oxygen atoms at shared corners, termed bridging oxygen atoms [17]. The proportion of bridging to non-bridging oxygen is contingent upon the composite's composition [17].

Several techniques deposit pure and doped ZnO thin films on different substrates, such as SILAR [18], chemical bath deposition [19], RF sputtering [20], sol-gel [21], combustion [22], and spray pyrolysis [23]. The sol-gel technique, among these, has advantages, being cost-effective, allowing high-purity deposition, and enabling the formation of homogeneous, large-area films at relatively low temperatures [24, 25]. The sol-gel technique suggests versatile potentials of making small, as well as decent adherence, wide-area coatings, with a complex-shaped substrate like the internal side of a pipe, which cannot be attained by other deposition technologies [26–28].

Taking into consideration all the features discussed above, it is essential to note that cadmium zinc tungsten phosphate where to the best of the author's knowledge after extensive surveys, cadmium zinc tungsten phosphate has not been fabricated as a diode. Consequently, the utilization of a combined matrix containing cadmium zinc tungsten phosphate through sol-gel processes reveals significant characteristics. These include the promotion of recombination within the junction, the introduction of innovative carrier valleys within the band gap, and an increase in carrier recombination in the trap states.

In this study, cadmium zinc tungsten phosphate thin film was meticulously prepared through controlled sol-gel and spin coating processes, showcasing advantageous characteristics such as a substantial surface area and a controlled

bandgap. The obtained powder was deposited by thermal vacuum evaporation. The comprehensive examination encompasses the microstructural, optical, and electrical properties of the resulting films. Additionally, the study entails the fabrication and electrical characterization of a cadmium zinc tungsten phosphate /Si diode.

2 Experimental work

2.1 Materials and preparation procedures

The cadmium zinc tungsten phosphate film preparation utilized a straightforward sol-gel process in ambient conditions. First, an acid solution was prepared by mixing 15 ml of 35% hydrochloric acid with 45 ml of distilled water. Triethyl phosphate (99.8%, Merck) was used as a source of phosphate, and zinc-acetate (93%, PubChem), cadmium nitrate (99%, PubChem), and tungsten chloride (98%, PubChem) salts solutions were then individually prepared and combined. This mixture underwent magnetic stirring for 1 h. A modified sol-gel process was applied for the phosphate-based solution. After aging overnight, the cadmium zinc tungsten phosphate films were formed by spin-coating the solution onto glass and silicon substrates at 1500 rpm for 30 s. Subsequently, the films were calcined at 400°C for 1 h. For I-V electrical measurements, metallic electrodes were deposited on the upper and lower surfaces of the cadmium zinc tungsten phosphate/p-Si heterostructure diode, with silver paste and thermally deposited aluminum (Al), respectively.

2.2 Characterization

Structural analysis of cadmium zinc tungsten phosphate film was conducted using a D8-Bruker Advance X-ray diffractometer with CuK α radiation (40 kV, 40 mA). This instrument unveiled the crystal structure. For high-resolution morphology observations, Scanning Electron Microscopy (Quanta FEG-250 at 20 kV) was employed, providing detailed imaging of the film's surface and structure. Optical properties spanning 190 to 1500 nm were explored using a JASCO V-570-UV-VIS-NIR spectrophotometer, measuring light absorption, transmission, and reflection characteristics. To investigate the dark current-voltage (I-V) characteristics of the cadmium zinc tungsten phosphate/p-Si heterojunction at different temperatures, a gold layer was evaporated onto CZPW through a mask to form a front ohmic electrode, and another gold layer was evaporated onto p-Si as a back electrode, resulting in the Au/CZWP/p-Si/Au heterojunction. For electrical property measurement, copper wires were equipped with thermosetting silver paint and mechanically applied to the two metal electrodes for dark current-voltage

(I–V) measurements at different temperatures using a KEY-SIGHT B 2901A source meter.

3 Results and discussions

3.1 Structure analysis

Figure 1 illustrates the X-ray diffraction (XRD) pattern of a zinc cadmium tungsten phosphate (28: 22: 5: 45) sample prepared using the sol–gel method. The observed diffraction peaks closely correspond to those of monoclinic $\text{Zn}_2\text{P}_2\text{O}_7$ (JCPDS: 96–231-0788), and also the same peaks correspond to the $\text{Cd}_2\text{P}_2\text{O}_7$ (JCPDS: 96–220-8749). This observation suggests that the formation of $(\text{Cd}_{0.4}\text{Zn}_{0.6})_2\text{P}_2\text{O}_7$ where Zn

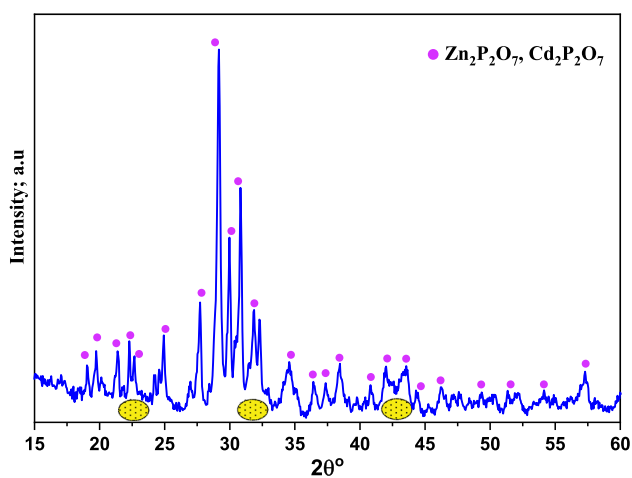


Fig. 1 XRD spectrum of zinc cadmium tungsten phosphate film

and Cd are in the same group therefore, they can replace each other in the crystal structure with a small distortion in the lattice parameters due to the difference in the ionic radius. The XRD pattern doesn't show additional peaks for other phases. Upon closer examination, the zinc cadmium tungsten phosphate sample exhibits sharp peaks at (2θ) 29° and 30.8°, indicating good crystallinity. However, there is splitting in the diffraction peaks at (2θ) 22.2°, 31.8°, and 42°, accompanied by slight broadening, suggesting a smaller crystallite size.

This phenomenon could be attributed to a higher change in the atomic fraction within the lattice of zinc cadmium tungsten phosphate owing to the notable difference in the ionic radii of Cd^{2+} (0.97 Å), Zn^{2+} (0.74 Å), W (1.41 Å), and P^{5+} (1.23 Å). The sol–gel synthesis, followed by calcination at 400°C, results in spontaneous combination and product formation, contributing to the observed diffraction patterns. The average crystallite size is determined to be 39.30 nm.

3.2 Morphology

The FESEM image presented in Fig. 2 provides insight into the morphology of the synthesized nanograpes structures of cadmium zinc tungsten phosphate. The SEM analysis unveils the nanoporous morphology of the cadmium zinc tungsten phosphate nanostructure, showcasing a successfully formed crystalline structure. In the presence of grapes-like structures exhibiting a high degree of cross-linkage, these grapes-like structures spontaneously self-assemble, forming a dense nanostructure. Also, the aggregation in cadmium zinc tungsten phosphate refers to the tendency of these structures to clump together, often due to various factors such as the surface chemistry of P_2O_5 in the system because of

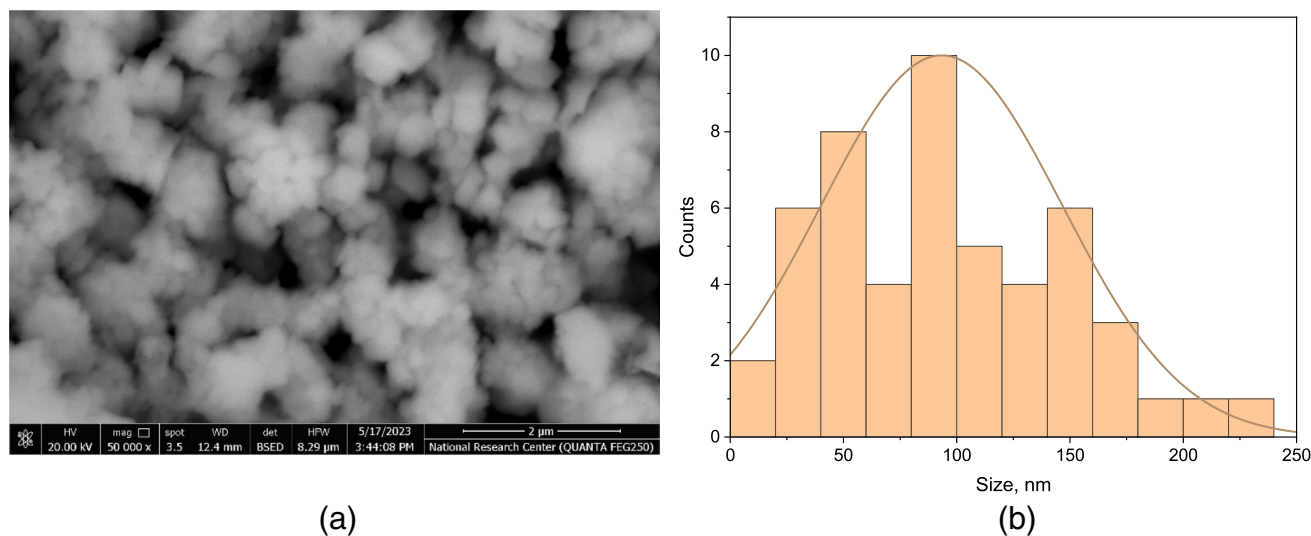


Fig. 2 a FE-SEM of zinc cadmium tungsten phosphate and b particle distribution

their higher ability to absorb OH form their surrounding environmental conditions [29–33]. Figure 2(b) illustrates grapes-like structures with particles having average diameters within the range of 100 nm.

3.3 Optical properties

In the field of material science, the intricate interplay between light and matter yields crucial insights into the fundamental nature of substances. UV–Visible spectroscopy, standing out among numerous techniques, serves as a robust and indispensable tool for the in-depth exploration of electronic structure and band gap phenomena. Photons' interactions with matter, whether absorption, transmission, or reflection, manifest distinct spectral features [24, 25, 34, 35].

Figure 3 illustrates the optical transmission and reflectance characteristics of zinc cadmium tungsten phosphate film, approximately 1.8 μm in thickness. The observations reveal a light increase in transmittance by increasing wavelength with a transmittance peak at about 282 nm. The shows low values with nearly no change beyond that range.

The computation of the absorption coefficient (α) was executed utilizing the model [36]:

$$\alpha t = \ln\left(\frac{(1-R)^2}{T}\right) \quad (1)$$

In this context, "t" signifies film thickness, "R" denotes reflection, and "T" represents transmission. Figure 4 elucidates the correlation between the zinc cadmium tungsten phosphate film's absorption coefficient and wavelength, demonstrating a progressive escalation, attaining its zenith at about 282 nm, while sustaining transparency within the measured range.

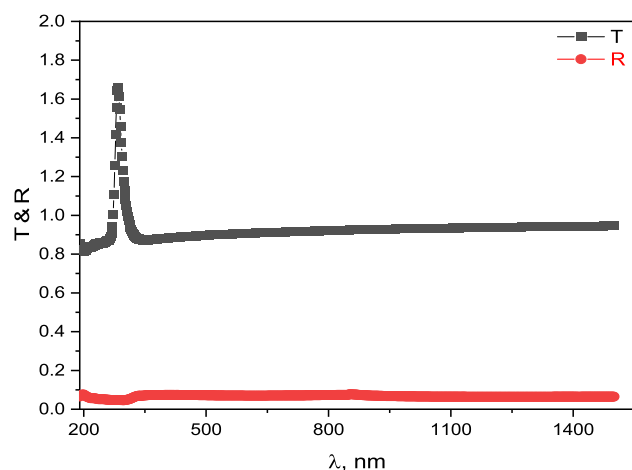


Fig. 3 The optical transmission and reflectance characteristics of zinc cadmium tungsten phosphate film

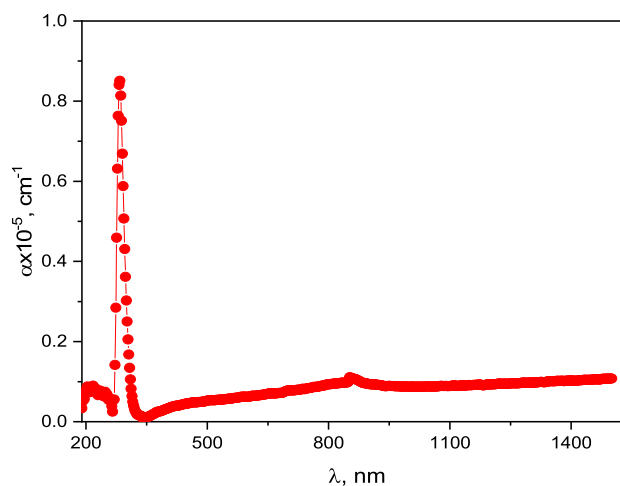


Fig. 4 The correlation between the zinc cadmium tungsten phosphate film's absorption coefficient and wavelength

Undoped ZnO–CdO–P₂O₅ composites and glasses undergo charge transfer spectral analysis. Metal impurities like Fe, Ni, W, and Cr ions, present in raw materials, play a crucial role in UV absorption [37]. The charge transfer spectrum is attributed to electron transfer, specifically the transition from the coordinated oxygen orbital to the cation orbital [37]. Credible experimental findings [38, 39] provide unassailable evidence supporting the hypothesis that the sharp UV absorption bands observed in various phosphate compounds result from impurities present in the raw materials employed during the preparation process. This postulation serves as a fundamental explanation for the notable UV absorption observed in the ZnO–CdO–P₂O₅ composites. The absorption phenomena observed in the CdO–ZnO–P₂O₅ host, induced by 3d transition metal (TM) ions, find roots in either lower valence states or the fascinating induction of octahedral coordination facilitated by the phosphate host medium. Noteworthy is the absorption spectrum of WO-doped samples, unveiling a significant peak at about 282 nm. This empirical evidence underscores the prevalence of dominant octahedral coordination featuring divalent tungsten ions [40].

The determination of the optical band gap of the CZWP film is achieved through the application of the absorption coefficient α , elucidated by the equation [4, 10]:

$$\alpha h\nu = A(h\nu - E_g)^n \quad (2)$$

where E_g signifies the energy gap, $h\nu$ denotes photon energy, A is a constant, and the exponent value (n) takes the specific values of 2 for allowed indirect transitions and 1/2 for allowed direct transitions [4]. Ascertain the band gap by extending the linear section of the Tauc plots to the energy axis when the absorption coefficient (α) reaches zero [41].

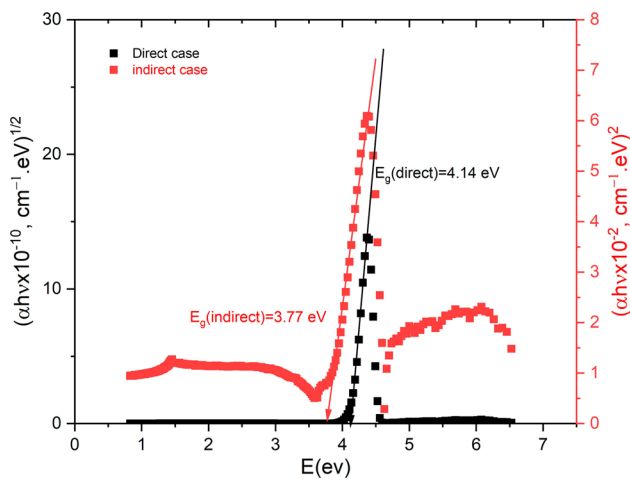


Fig. 5 Tauc plots of the zinc cadmium tungsten phosphate film's

The plots in Fig. 5 showcase striking linearity, suggesting the coexistence of both indirect (3.77 eV) and direct (4.14 eV) band gaps in the films. Notably, the higher probability of the indirect gap positions it favorably for photovoltaic applications [42]. These outcomes align with observations in cadmium zinc phosphate [43, 44], other studies on CdO and ZnO composites [45–52], and also with cadmium phosphate [53–55] or zinc phosphate [56]. Chawla et al. investigated the UV–visible spectroscopic characteristics of CdZnS nanoparticles [57]. Remarkably, their analysis of the UV–visible spectrum and Tauc plot confirmed the increased band gap of 3.59 eV. Ibrahim et al. examined the influence of cadmium (Cd) on the estimation of zinc phosphate using UV–Vis spectra. They observed a slight decrease in the estimated value, from 3.68 to 3.2 eV, with increasing CdO content [58]. Hence, the resulting band gap of zinc cadmium tungsten phosphate film typically falls within a certain range, influenced by various factors such as composition, crystalline structure, and synthesis method.

Both the refractive index (n) and extinction coefficient are pivotal in optical considerations. The determination of the films' refractive index (n) involved applying the following relationship [59]:

$$n = ((1 + R/1 - R) + \sqrt{(4R/(1 - R)^2) - K^2}) \tag{3}$$

Here, (K) represents the extinction coefficient.

In Fig. 6, the variation of the refractive index (n) with increasing wavelength unfolds. A notable observation is the refractive index stays nearly unchanged with increasing wavelength. The refractive index's significance extends to designing communication devices, optical materials, lithography, imaging, and solar devices [60].

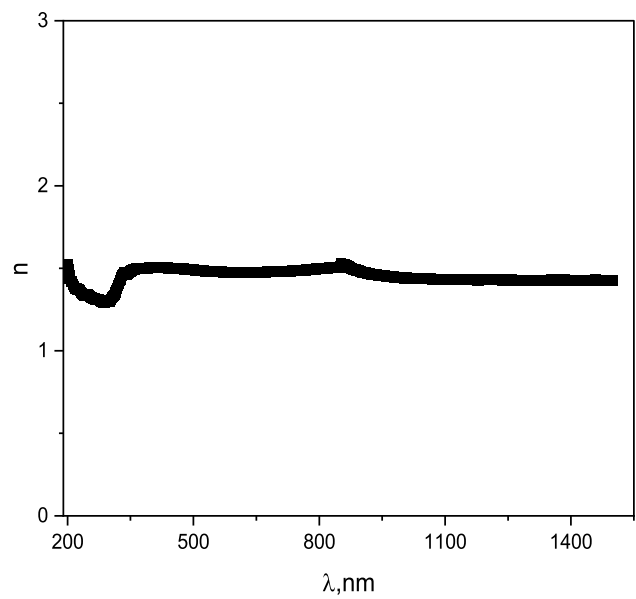


Fig. 6 The variation of the refractive index (n) with increasing wavelength of the zinc cadmium tungsten phosphate film's

Compute the optical conductivity ($\sigma_{optical}$) of cadmium zinc tungsten phosphate nanocomposite films using the equation [61]:

$$\sigma_{optical} = \alpha nc/4\pi \tag{4}$$

Examine the variation of optical conductivity with incident ray wavelength in Fig. 7a. The observed trend showcases an increase, reaching a maximum at approximately 282 nm, aligning with the previously observed peak absorption. Subsequently, a decrease follows, directly correlated with the optical density illustrated in Fig. 7b. Enhanced optical conductivity can be attributed to the heightened excitation state of electrons, stemming from increased energies of incident rays and the augmented absorption coefficient of the films [2, 62].

Utilize the next equation [63] to determine the optical electronegativity (η) in cadmium zinc tungsten phosphate nanocomposite films, incorporating refractive index (n) and dimensionless constant (A):

$$\eta_{optical} = (A/n)^{0.25} \tag{5}$$

Explore the visual representation in Fig. 8, illustrating the fluctuation of optical electronegativity concerning incident ray wavelengths. Witness a steady state, peaking around 282 nm, mirroring patterns observed in absorption coefficient, optical conductivity, and optical density. This coherence underscores the interconnected nature and significance of these parameters within cadmium zinc tungsten phosphate nanocomposite films.

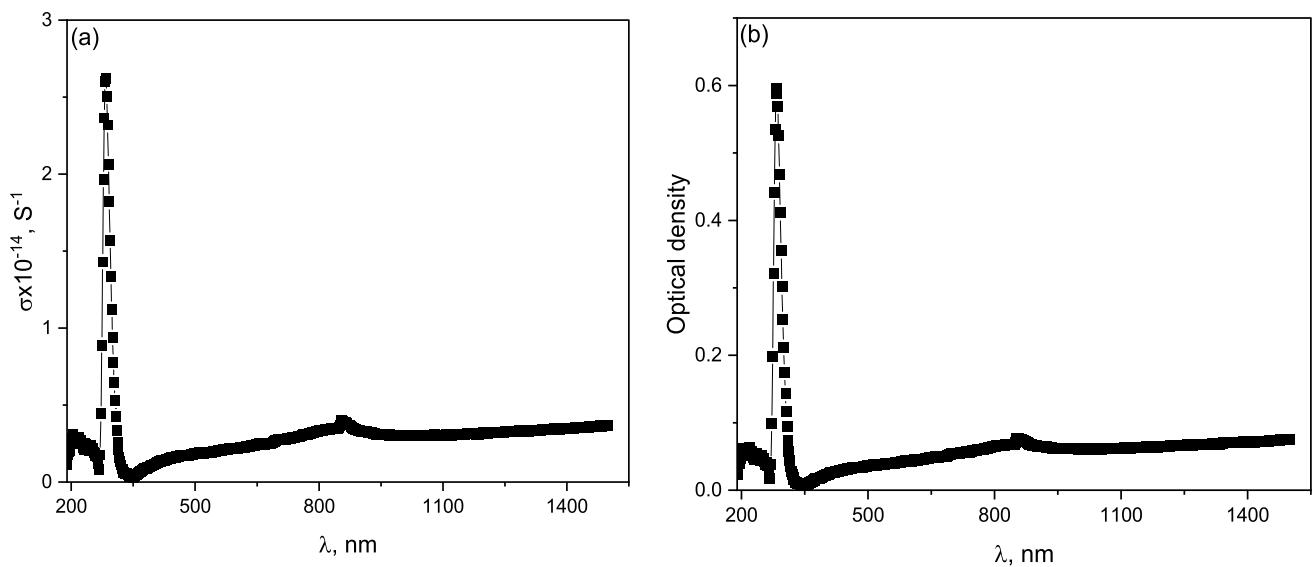


Fig. 7 The variation of (a) optical conductivity and (b) optical density with incident ray wavelength

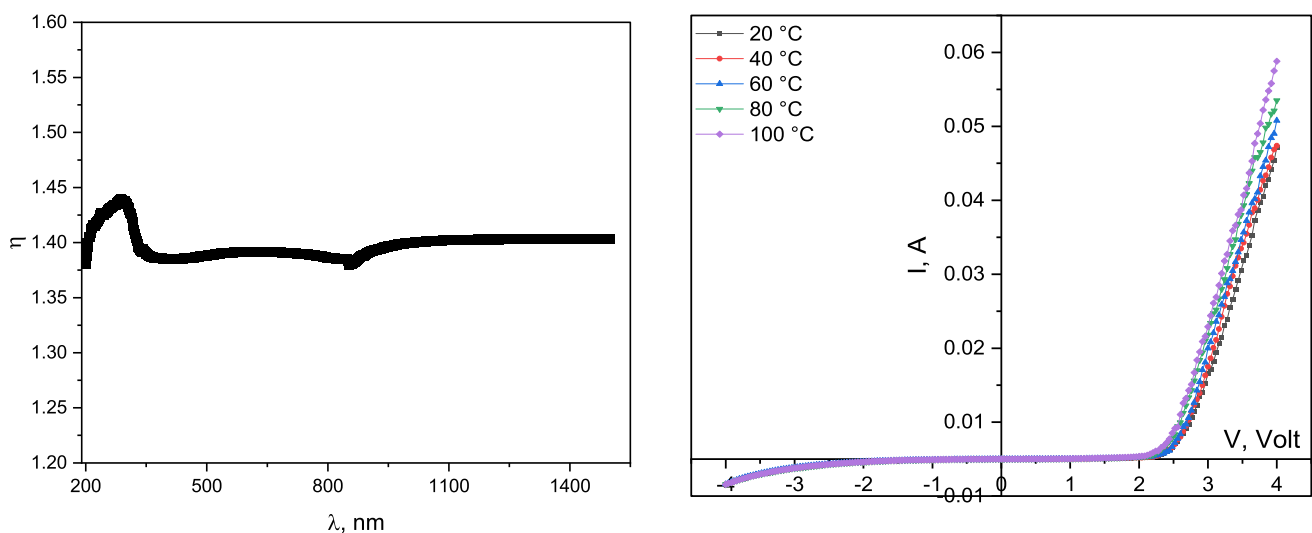


Fig. 8 The variation of optical electronegativity (η) with incident ray wavelength

3.4 Dark I-V-T characteristics of Cadmium Zinc Tungsten Phosphate/p-Si Heterojunction

The I-V characteristics of the cadmium zinc tungsten phosphate/p-Si heterojunction (HJ) are meticulously presented in Fig. 9. Observed at various temperatures and ± 4 V applied potentials, the graph illustrates a potential barrier at the interface of the p-Si and CZNP layers, exemplifying diode-like behavior. Notably, the introduction of tungsten significantly enhances the rectification performance.

Fig. 9 The I-V characteristics of the cadmium zinc tungsten phosphate/p-Si heterojunction

It is crucial to investigate the I-V characteristics at dark to unveil transport mechanisms and extract diode parameters. Notably, Fig. 9 discloses a significant finding: the forward current demonstrates dual behaviors. Below 0.7 V, it follows a linear trend; beyond this limit, it takes an alternate route, deviating from the linear pattern. This phenomenon is attributed to the formation of series resistance at the layer interface [64].

In Fig. 10, the natural logarithm of forward current ($\ln I$) versus applied junction voltage unveils a linear trend at low potentials ($V \leq 0.7$ V) and a curved shape at higher potentials (0.7 V $< V \leq 4$ V). This curvature results from resistances

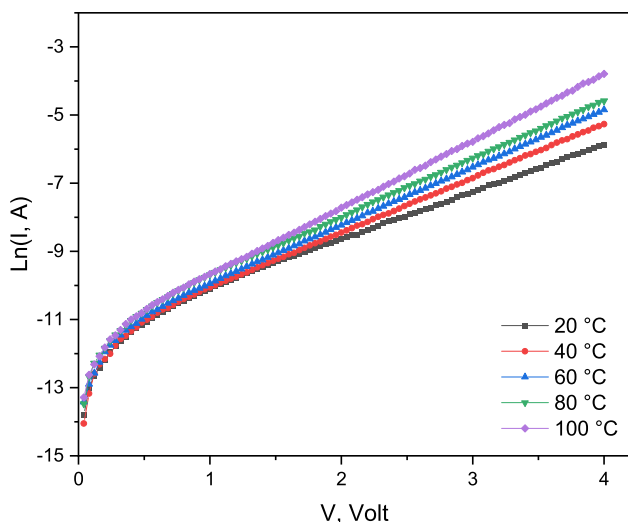


Fig. 10 The natural logarithm of forward current (ln I) versus applied junction voltage

introduced during cadmium zinc tungsten phosphate/p-Si and wiring processes, forming the series resistance (Rs) [65].

The dark forward current is adjusted in the relatively low voltage range (below 0.7 V) through the application of thermionic emission theory. As per this theory, the electrical current passing through the junction corresponds to the applied voltage [66] as:

$$\frac{I}{I_0} = \left[\exp\left(\frac{qV}{nK_B T}\right) \right] - 1 \tag{6}$$

The equation relates the current (I) to the reverse direction saturation current (I₀). In this equation, q represents charge, V is the applied voltage, n is the ideality factor, K_B is Boltzmann's constant, and T is the absolute temperature. The reverse saturation current (I₀) can be ascertained through the application of the following equation [67]:

$$I_0 = AA^* \cdot \exp(q\phi/K_B T) \tag{7}$$

Representing key device parameters, A, A*, and φ signify the effective area, Richardson constant (p-Si) = 32, and the effective barrier height at zero-biasing, respectively [68].

On a semi-log plot (Fig. 10), the linear part (V ≤ 0.7 V) estimates junction ideality factor (n) and barrier height (φ) [69].

$$nK_B T = e \left(\frac{dV}{d \ln I} \right) \tag{8}$$

Table 1 n, φ (from I-V characteristics and from Norde's plot), and the calculated Rs

T, K	n	φ, eV (from I-V)	Rs, KΩ	φ, eV (from Nord)
293	11.37	0.69	1.442	0.85
313	10.69	0.74	1.411	0.88
333	10.52	0.79	1.28	0.91
353	10.34	0.83	1.21	0.95
373	9.92	0.88	0.99	0.97

$$\frac{q\phi}{K_B T} = \ln\left(\frac{AA^* T^2}{I_0}\right) \tag{9}$$

Table 1 provides data on ideality factor and barrier height extracted from the I-V curve (V ≤ 0.7 V) using thermionic emission. Additionally, observe the temperature-dependent trends in Fig. 11, where the ideality factor decreases and the barrier height increases.

The data suggests a diode ideality factor above one, signifying a non-ideal heterojunction. This results from an electron-hole combination in the interface. Additionally, rising temperature decreases n, while the barrier height undergoes lateral variation [70].

Current easily navigates low barriers at lower temperatures. However, with rising temperatures, electrons gather enough energy to overcome higher barriers, resulting in an elevation of barrier height at every temperature and applied voltage. The temperature-dependent barrier height in cadmium zinc tungsten phosphate/p-Si can be ascribed to factors like tunneling, series resistance, variations in barrier height, and interfacial states [71].

Recognized as a significant influencer of junction characteristics, series resistance (Rs) can be determined through the

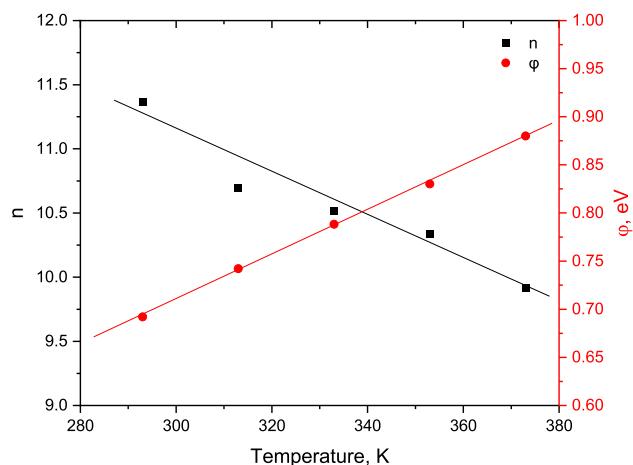


Fig. 11 The temperature-dependent trends of both the ideality factor and barrier height of the junction

application of the modified Norde's equation. This method stands as a reliable approach for calculating the value of diode series resistance [72].

$$F(V) = \frac{V}{Y} - \frac{k_B T}{e} \left(\ln \left(\frac{I(V)}{AA^* T^2} \right) \right) \tag{10}$$

Y signifies the smallest integer greater than the acknowledged ideality factor.

Figure 12 illustrates Norde's equation, presenting the derivation of series resistance (Rs) [73].

$$R_s = \frac{k_B T(Y - n)}{eI(V_0)} \tag{11}$$

The current represented by I(Vo) is equivalent to the voltage at the bottom of the F(V) curvature. The Norde equation [74] offers a systematic approach for acquiring the barrier height:

$$\phi = F(V_0) + \frac{V_0}{Y} - \frac{k_B T}{e} \tag{12}$$

Vo, signifying the voltage at this juncture, corresponds to the lowest point on the F(V) curve, denoted by F(Vo).

Utilizing Eqs. 11 and 12 on Norde's plot yields Rs and φ, and these values populate Table 1. Comparing barrier heights from I-V data and Norde's method, the slight variations are attributed to distinct mathematical approaches. The table highlights a declining Rs with increasing temperature, attributed to enhanced charge carrier mobility at the interface.

To understand charge transport across the cadmium zinc tungsten phosphate/p-Si junction, analyzing the I-V characteristics at voltages beyond 0.7 V is crucial. Figure 13 illustrates this with a double log-log plot, showing a

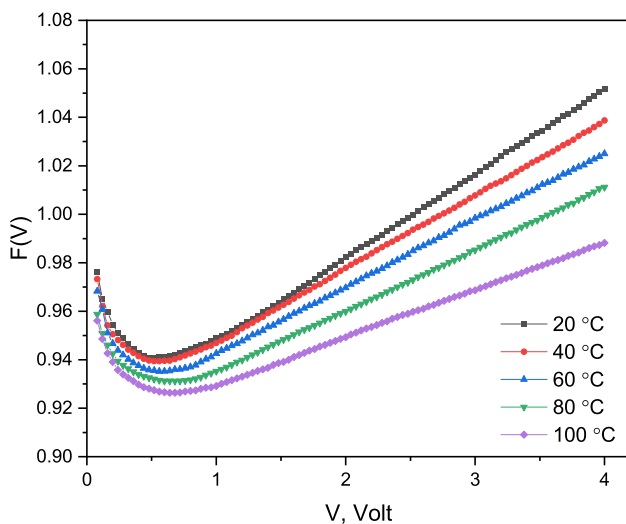


Fig. 12 Norde's equation of the junction

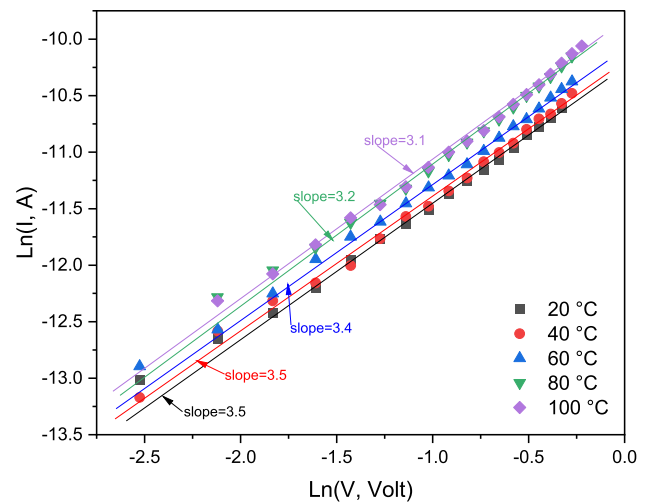


Fig. 13 A double log-log plot of the junction

power-dependent, space charge-limited current dominated by an exponential trap distribution.

In Fig. 14, a meticulous observation reveals the temperature-dependent behavior of reverse current (IR) at different voltages. This slight increase with rising temperature suggests the involvement of multiple transport mechanisms. Notably, carrier generation and recombination emerge as significant factors influencing junction losses within the Silicon substrate [1, 75].

$$I_R = I_s e^{\Delta E / k_b T} \tag{13}$$

The carrier activation energy (ΔE), as derived from Eq. (13), is about 1.28 electron volts.

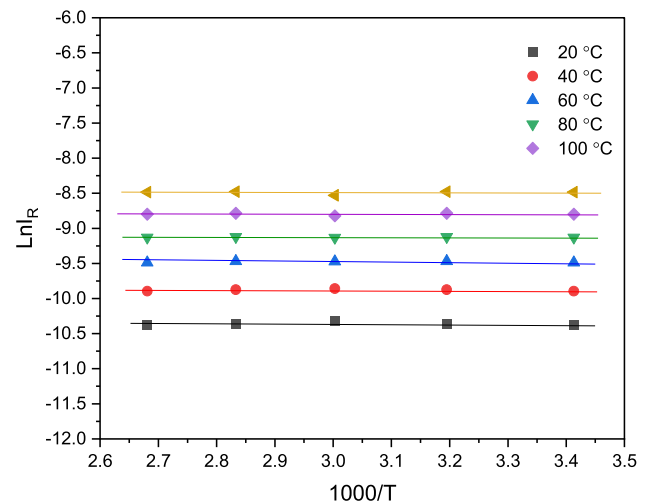


Fig. 14 The temperature-dependent behavior of reverse current (IR) at different voltages

Finally, in comparison to previous work on the cadmium zinc nickel phosphate/p-Si diode [76], the ideality factor of the current diode is higher than the cadmium zinc nickel phosphate/p-Si diode. While the barrier heights of both diodes are nearly. These notes tell us that the doping cadmium zinc phosphate with nickel is more effective than tungsten in electronic junction fabrication.

4 Conclusion

The sol–gel spin coating method effectively facilitated W-doped CZP thin film growth on glass and p-Si substrates. The XRD analysis reveal a single-phase monoclinic structure for Zn₂P₂O₇ and Cd₃P₆O₂₈, with sharp peaks at 2θ 29.0 and 30.8, indicating excellent crystallinity. SEM analysis reveals a nanoporous morphology in the cadmium zinc tungsten phosphate nanostructure, demonstrating successful crystalline structure formation. Nanograpes structures, characterized by significant cross-linkage, spontaneously self-assemble into nanoclusters, ultimately leading to the formation of dense nanostructures. Microstructure analysis conclusively confirmed that the combination of Zn, Cd, P₂O₅, and W doping yielded tailored and homogeneous nanomaterials. The absorption spectra of 3d transition metal (TM) ions in the CdO-ZnO-P₂O₅ host hinted at the presence of TM ions in lower valence states, suggesting octahedral coordination influenced by the phosphate host medium. Particularly, WO-doped samples showcased a distinctive absorption peak at 282 nm, affirming the dominant presence of divalent W ions in an octahedral coordination environment. Our microstructure analysis reaffirmed that when Zn and Cd ions combine with a phosphate-based nanostructure, they have the ability to form homogeneous nanomaterials. Optical absorption studies of CADMIUM ZINC TUNGSTEN PHOSPHATE films unveiled both direct and indirect energy gaps, measuring 3.77 and 4.14 eV, respectively. Additionally, the CADMIUM ZINC TUNGSTEN PHOSPHATE/p-Si characteristics were meticulously analyzed in dark modes, offering valuable insights into the transport ideality factor, barrier height, and series resistance of the device.

Acknowledgements The work was supported by grant number 13020232, and the National Research Centre of Egypt facilitates the work and the characterization tools

Author contributions All authors conceived and designed the experiments; Analyzed and interpreted the data; Contributed reagents, materials, analysis tools, or data; Wrote the paper.

Funding Open access funding provided by The Science, Technology & Innovation Funding Authority (STDF) in cooperation with The Egyptian Knowledge Bank (EKB).

Data availability Not available.

Declarations

Conflict of interest The authors declare no competing interests.

Ethics approval Not applicable.

Human participant and animal research This research doesn't involve Human Participants and/or Animals.

Consent to participate Authors confirm their participation.

Consent for publication The authors confirm their acceptance for Publication.

Open Access This article is licensed under a Creative Commons Attribution 4.0 International License, which permits use, sharing, adaptation, distribution and reproduction in any medium or format, as long as you give appropriate credit to the original author(s) and the source, provide a link to the Creative Commons licence, and indicate if changes were made. The images or other third party material in this article are included in the article's Creative Commons licence, unless indicated otherwise in a credit line to the material. If material is not included in the article's Creative Commons licence and your intended use is not permitted by statutory regulation or exceeds the permitted use, you will need to obtain permission directly from the copyright holder. To view a copy of this licence, visit <http://creativecommons.org/licenses/by/4.0/>.

References

1. A. M. Mansour, A. B. Abou Hammad, and A. M. El Nahrawy, *Nano-Structures and Nano-Objects* **25**, 100646 (2021).
2. A. B. Abou Hammad, A. M. Mansour, F. Cao, and A. M. El Nahrawy, *ECS Journal of Solid State Science and Technology* **10**, 103016 (2021).
3. H. Ishaq, I. Dincer, C. Crawford, *Int. J. Hydrogen Energy* **47**, 26238 (2022)
4. A. Elzawy, A.M. Mansour, H.S. Magar, A.B.A. Hammad, R.Y.A. Hassan, A.M. El Nahrawy, *Mater Today Commun* **33**, 104574 (2022)
5. Y. Wang, F. Wang, J. Zhou, H. Zhu, Q. Liao, L. Li, Y. Zhu, Y. Yuan, J. Zhang, *J. Alloys Compd.* **826**, 154225 (2020)
6. D. Ali, M.Z. Butt, I. Muneer, M.A. Farrukh, M. Aftab, M. Saleem, F. Bashir, A.U. Khan, *Thin Solid Films* **679**, 86 (2019)
7. Z.N. Kayani, N. Yaseen, S. Riaz, S. Naseem, *Mater Res Express* **5**, 36418 (2018)
8. V. Kumar, N. Singh, R.M. Mehra, A. Kapoor, L.P. Purohit, H.C. Swart, *Thin Solid Films* **539**, 161 (2013)
9. R. Demir, İ Kaya, *J. Mater. Sci.* **30**, 7103 (2019)
10. A. M. Mansour, A. B. Abou Hammad, A. M. Bakr, and A. M. El Nahrawy, *Silicon* **14**, 11715 (2022).
11. A. M. El Nahrawy, A. S. Montaser, A. M. Bakr, A. B. Abou Hammad, and A. M. Mansour, *Journal of Materials Science: Materials in Electronics* **32**, 28019 (2021).
12. A. M. El Nahrawy, A. B. Abou Hammad, A. M. Bakr, T. I. Shaheen, and A. M. Mansour, *Applied Physics A* **126**, 654 (2020).
13. D.C. Look, *Mater. Sci. Eng. B* **80**, 383 (2001)
14. A. Ohtomo, M. Kawasaki, T. Koida, K. Masubuchi, H. Koinuma, Y. Sakurai, Y. Yoshida, T. Yasuda, Y. Segawa, *Appl. Phys. Lett.* **72**, 2466 (1998)
15. Z.R. Munirah, M.S. Khan, Khan, and A. Aziz, *Materials Science-Poland* **32**, 688 (2014)

16. J.-Y. Chung, J.-H. Kim, S.-Y. Choi, H.-J. Park, M.-K. Hwang, Y.-K. Jeong, B.-K. Ryu, J.-Y. Chung, J.-H. Kim, S.-Y. Choi, H.-J. Park, M.-K. Hwang, Y.-K. Jeong, B.-K. Ryu, J. Korean Ceram. Soc. **52**, 128 (2015)
17. S. Chowdhury, P. Mandal, S. Ghosh, Mater. Sci. Eng. B **240**, 116 (2019)
18. S. Mondal, S.R. Bhattacharyya, P. Mitra, Pramana - Journal of Physics **80**, 315 (2013)
19. J. Xu, Y. Yu, X. He, J. Sun, F. Liu, G. Lu, Mater. Lett. **81**, 145 (2012)
20. G.M. Wu, Y.F. Chen, H.C. Lu, Acta Physica Polonica. Series A **120**, 149 (2011)
21. P. Sagar, M. Kumar, and R. M. Mehra, Materials Science-Poland **23**, (2005).
22. L.C. Nehru, V. Swaminathan, C. Sanjeeviraja, Powder Technol. **226**, 29 (2012)
23. S.D. Shinde, G.E. Patil, D.D. Kajale, V.B. Gaikwad, G.H. Jain, J. Alloys Compd. **528**, 109 (2012)
24. A. B. Abou Hammad, A. M. Mansour, and A. M. El Nahrawy, Phys Scr **96**, 125821 (2021).
25. A. M. El Nahrawy, A. B. Abou Hammad, and A. M. Mansour, Phys Scr **96**, 115801 (2021).
26. A.M. El Nahrawy, H.S. El-Deen, A.A. Soliman, W.M.M. Mosa, Egypt. J. Chem. **62**, 525 (2019)
27. A. M. El Nahrawy, A. S. Montaser, A. B. Abou Hammad, M. Ezzat, and M. El-shakankery, Silicon **12**, 1743 (2020).
28. A. M. Mansour, B. A. Hemdan, A. Elzawy, A. B. Abou Hammad, and A. M. El Nahrawy, Sci Rep **12**, 9855 (2022).
29. P. Kaur, K.J. Singh, A.K. Yadav, H. Sood, S. Kaur, R. Kaur, D.S. Arora, S. Kaur, Mater. Sci. Eng. C **83**, 177 (2018)
30. R. Catteaux, I. Grattepanche-Lebecq, F. Désanglois, F. Chai, J.C. Hornez, S. Hampshire, C. Follet-Houttemane, Chem. Eng. Res. Des. **91**, 2420 (2013)
31. A. Elnahrawy, A.B. AbouHammad, Int J Pharmtech Res **9**, 16 (2016)
32. F. Sharifianjazi, N. Parvin, M. Tahriri, J. Non Cryst. Solids **476**, 108 (2017)
33. A. M. El Nahrawy, A. B. Abou Hammad, and A. M. Mansour, Silicon **13**, 3733 (2021).
34. A. M. El Nahrawy, A. M. Mansour, A. B. Abou Hammad, R. S. Ibrahim, A. M. Abouelnaga, and M. S. Abdel-Aziz, J Inorg Organomet Polym Mater **30**, 3084 (2020).
35. A. M. El Nahrawy, A. Elzawy, A. B. Abou Hammad, and A. M. Mansour, Solid State Sci **108**, 106454 (2020).
36. A. Özmen, Y. Yakar, B. Çakir, Ü. Atav, Opt. Commun. **282**, 3999 (2009)
37. F. G. K. Baucke, J. Duffy, and D. Köpsel, 269 (2001).
38. A. Xiao, Y. Liu, T. Yang, W. Jia, X. Song, Y. Qian, C. Liang, and T. Ma, Acta Mater **245**, (2023).
39. J. Husband, F. Aguirre, C.J. Thompson, R.B. Metz, Chem. Phys. Lett. **342**, 75 (2001)
40. F.H. ElBatal, M.A. Marzouk, H.A. ElBatal, I.M. Elkashef, J. Electron. Mater. **51**, 3248 (2022)
41. A.M. Mansour, E.M. El-Menyawy, G.M. Mahmoud, Int. J. Microstruct. Mater. Prop. **14**, 272 (2019)
42. S. Joishy, B.V. Rajendra, A. Rao, S.D. Kulkarni, J. Mater. Sci. Mater. Electron. **28**, 7489 (2017)
43. M.A. Ghauri, J. Mater. Sci. Lett. **2**, 660 (1983)
44. C.A. Hogarth, M.A. Ghauri, J. Mater. Sci. **14**, 1641 (1979)
45. D. Ponnusamy, A.K. Prasad, M. Sridharan, Microchim. Acta **183**, 311 (2016)
46. H. Karami, Int. J. Electrochem. Sci. **5**, 720 (2010)
47. K. Karthik, S. Dhanuskodi, C. Gobinath, S. Sivaramkrishnan, Spectrochim Acta A Mol Biomol Spectrosc **139**, 7 (2015)
48. A. Yousef, N.A.M. Barakat, T. Amna, A.R. Unnithan, S.S. Al-Deyab, and H. Yong Kim, J Lumin **132**, 1668 (2012)
49. A.A. Ziabari, F.E. Ghodsi, J. Alloys Compd. **509**, 8748 (2011)
50. P.S. Kumar, M. Selvakumar, P. Bhagabati, B. Bharathi, S. Karuthapandian, S. Balakumar, RSC Adv. **4**, 32977 (2014)
51. L.J. Zhou, C. Li, X. Zou, J. Zhao, P.P. Jin, L.L. Feng, M.H. Fan, G.D. Li, Sens Actuators B Chem **197**, 370 (2014)
52. E. Mosquera, I. Del Pozo, M. Morel, J. Solid State Chem. **206**, 265 (2013)
53. M.A. Ghauri, F.M. Nazar, W.H. Bokhari, J. Non Cryst. Solids **46**, 197 (1981)
54. D.D. Souza, J. Nettar, K.P. Nagaraja, AIP Conf. Proc. **2244**, 030001 (2020)
55. M.A. Ouis, M.A. Azooz, H.A. ElBatal, J. Non Cryst. Solids **494**, 31 (2018)
56. W. Mao, M. Cai, W. Xie, P. Li, S. Xu, J. Zhang, J. Am. Ceram. Soc. **103**, 1864 (2020)
57. D. Chawla, N. Goswami, Mater Today Proc **28**, 278 (2020)
58. S. E. Ibrahim, I. A. El-Mesady, M. M. Semaary, and S. M. Othman, Radiation Physics and Chemistry **209**, (2023).
59. A.M. Mansour, I.M. El Radaf, Int. J. Microstruct. Mater. Prop. **14**, 419 (2019)
60. A.M. Mansour, I.M. El Radaf, G.M. Mahmoud, Int. J. Microstruct. Mater. Prop. **14**, 462 (2019)
61. A.M. Mansour, E.M. El-Menyawy, G.M. Mahmoud, A.A. Azab, F.S. Terra, Mater Res Express **4**, 115903 (2017)
62. A. M. el nahrawy, A. I. Ali, A. B. Abou Hammad, and A. Mbarek, Egypt J Chem **61**, 1073 (2018).
63. A.M. Mansour, R.S. Ibrahim, A.A. Azab, J. Mater. Sci. Mater. Electron. **33**, 10251 (2022)
64. A. M. El Nahrawy, A. B. Abou Hammad, and A. M. Mansour, Arab J Sci Eng **46**, 5893 (2021).
65. A.M. ElNahrawy, A.M. Mansour, H.A. ElAttar, E.M.M. Sakr, A.A. Soliman, A.B.A. Hammad, J. Mater. Sci. Mater. Electron. **31**, 6224 (2020)
66. A.M. Mansour, S.A. Gad, A.M. Moustafa, G.M. Mahmoud, SILICON **14**, 2189 (2022)
67. I.M. El Radaf, A.M. Mansour, G.B. Sakr, J. Semicond. **39**, 124010 (2018)
68. M. Nasr, A.M. Mansour, I.M. El Radaf, Mater Res Express **6**, 036405 (2018)
69. A.M. Mansour, M. Nasr, H.A. Saleh, G.M. Mahmoud, Appl. Phys. A **125**, 1 (2019)
70. M.M. Toraya, A.M. El Nahrawy, A.M. Mansour, D.M. Atia, N.M. Ahmed, S. Hussin, SILICON **14**, 10837 (2022)
71. N. Hassan, A.M. Mansour, N. Roushdy, A.A.M. Farag, W.G. Osiris, Optik (Stuttg) **158**, 1255 (2018)
72. I.T. Zedan, E.M. El-Menyawy, A.M. Mansour, SILICON **11**, 1693 (2019)
73. A.M. Mansour, SILICON **11**, 1989 (2019)
74. N.A.A. Elkanzi, A.A.M. Farag, N. Roushdy, A.M. Mansour, Optik (Stuttg) **216**, 164882 (2020)
75. A.A.M. Farag, A.M. Mansour, A.H. Ammar, M.A. Rafea, A.M. Farid, J. Alloys Compd. **513**, 404 (2012)
76. A.B.A. Hammad, A.M.E. Nahrawy, A.M. Mansour, SILICON **1**, 1 (2023)

Publisher's Note Springer Nature remains neutral with regard to jurisdictional claims in published maps and institutional affiliations.